



ORIGINAL PAPER

George Z. Voyiadjis · Yooseob Song

# A physically based constitutive model for dynamic strain aging in Inconel 718 alloy at a wide range of temperatures and strain rates

Received: 9 April 2019 / Revised: 11 July 2019 / Published online: 27 September 2019  
© Springer-Verlag GmbH Austria, part of Springer Nature 2019

**Abstract** Dynamic strain aging has a huge effect on the microstructural mechanical behavior of Inconel 718 high-performance alloy when activated. In a number of experimental researches, significant additional hardening due to the dynamic strain aging phenomenon was reported. A constitutive model without considering dynamic strain aging is insufficient to accurately predict the material behavior. In this paper, a new constitutive model for Inconel 718 high-performance alloy is proposed to capture the additional hardening, which is caused by dynamic strain aging, by means of the Weibull distribution probability density function. The derivation of the proposed constitutive relation for the dynamic strain aging-induced flow stress, the athermal flow stress and the thermal flow stress is physically motivated. The developed model is applied to Inconel 718 high-performance alloy to demonstrate its ability to capture the dynamic strain aging behavior, which was observed in the literature across a wide range of temperatures (300–1200 K) and strain rates from quasi-static loading (0.001/s) to dynamic loading (1100/s).

## 1 Introduction

Inconel 718 is one of the most widely used nickel-based high-performance alloys (superalloy) used in heated sections of gas turbines and jet engines in aerospace industry due to its corrosion, wear and fatigue resistances as well as its high strength and ductility at elevated temperatures [1]. However, due to its chemical reaction with materials of cutting tools, work hardening behavior and poor thermal diffusivity, this material is very hard to cut. In spite of many studies on the surface integrity of workpieces and wear mechanisms of cutting tools, which are two major issues in cutting Inconel 718, there is still a need to research these issues.

Meanwhile, the dynamic strain aging (DSA) phenomenon is known as one of the key factors to determine the mechanical behavior of Inconel alloys. Macroscopically, dynamic strain aging (DSA) is explained as an abrupt intensification of the flow stress at a specific range of temperature. In general, flow stress decreases with increasing temperature. However, at certain combinations of temperature and strain rate, the flow stress tends to increase as the temperature rises and also tends to decrease back again after reaching a peak (see Figs. 1 and 2 for example). As shown in Figs. 1 and 2, the peak of flow stress is dependent on the strain level and the strain rate applied. The temperature range where DSA is activated also depends on the applied strain rate. The combinations of strain rate and temperature that lead to DSA change dramatically according to the crystal structure. Even within the same structure, it differs from material to material. Nemat-Nasser

---

G. Z. Voyiadjis (✉) · Y. Song  
Department of Civil and Environmental Engineering, Computational Solid Mechanics Laboratory, Louisiana State University,  
Baton Rouge, LA 70803, USA  
E-mail: voyiadjis@eng.lsu.edu

Y. Song  
Department of Civil Engineering, University of Texas Rio Grande Valley, Edinburg, TX 78539, USA

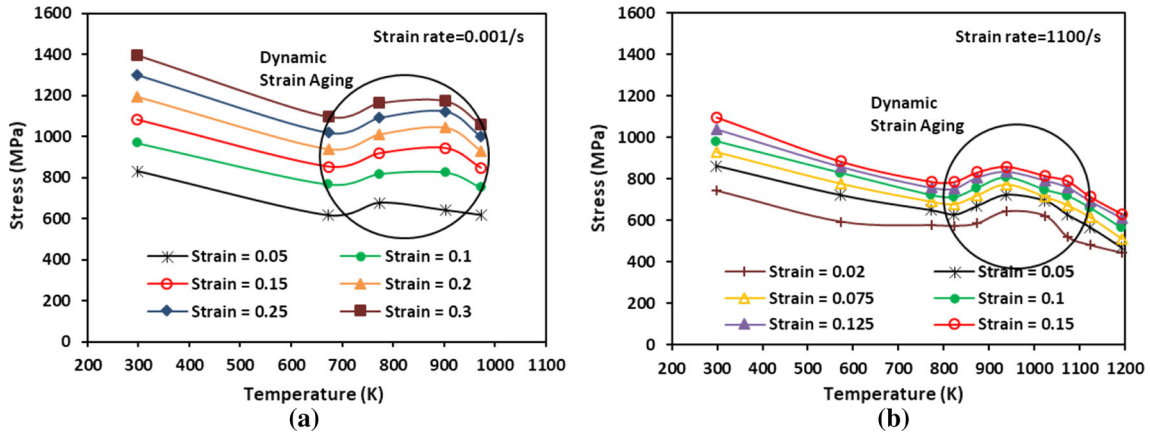


**Fig. 1** Flow stress versus temperature curves from experiments [7] according to the different strain levels with varying strain rates ( $\dot{\epsilon}$ ): **a**  $\dot{\epsilon} = 0.001/s$  and **b**  $\dot{\epsilon} = 1100/s$

and his co-workers [2,3] carried out extensive experiments to investigate the thermo-mechanical behavior of face-centered cubic (fcc) metals and body-centered cubic (bcc) metals including the DSA phenomenon over a wide range of strain rates and temperatures. In their experiments, DSA is observed only in the low strain rate range ( $\dot{\epsilon} \sim 10^{-3}/s$ ) when combined with the temperature range ( $T = 450-700$  K) in the case of niobium, whereas, in OFHC copper, vanadium and tantalum, DSA does not activate at all for the range of the strain rates  $\dot{\epsilon} = 10^{-3}-10^{-5}$  s and temperatures  $T = 77-1000$  K.

Inconel 718 superalloy contains diverse crystal lattices, e.g., face-centered cubic (fcc), body-centered cubic (bcc) and hexagonal close packed (hcp), as shown in Table 1 [4]. In addition, this material has an austenite fcc matrix  $\gamma$  phase as well as secondary phases such as a  $\gamma'$  phase based on  $Ni_3(Al, Ti)$ ; a gamma  $\gamma''$  phase body-centered tetragonal (bct) ordered  $Ni_3Nb$ ; etc. [4]. Mulford and Kocks [5] extensively studied the presence of DSA in Inconel 600. To demonstrate the instantaneous strain rate sensitivity on DSA, elevated temperature-strain rate experiments were conducted in their work. The DSA behavior in Inconel 718 was investigated in [6]. In [6], the serrated flow due to DSA, as a function of microstructural characteristics of Inconel 718, was reported over a wide range of temperatures ( $T = 473-973$  K) with a strain rate of  $\dot{\epsilon} = 6.5 \times 10^{-5}/s$ . From a literature review on Inconel alloys, especially on Inconel 718, one can observe that there is a lack of constitutive models suitable for DSA even though it is very important to consider it in order to accurately predict material responses when DSA becomes active.

In this work, a new constitutive model for capturing DSA in Inconel 718 is proposed based on the previous works by Voyiadjis and co-workers [8-10], and termed the Voyiadjis-Abed-Song (VAS) model. In [8], the physically based constitutive model for bcc was proposed. The current work proposes the combined constitutive model of bcc and fcc to address the modeling of DSA in Inconel alloys since the microstructural components of Inconel 718 contain two types of crystal structures, fcc and bcc, as shown in Table 1 (hcp is negligible in this alloy). The proposed VAS model is then validated using the experimental data which were presented by [7]. The DSA phenomenon observed in the experiments for Inconel 718 [7] is briefly reviewed in Sect. 2. The formulations of athermal, thermal and DSA elements of the flow stress in the VAS model are introduced in Sect. 3. In Sect. 4, to acquire the parameters for the VAS model, calibration is carried out using the experimental measurements conducted by [7]. The stress-strain behavior is considered to investigate the DSA phenomenon through the VAS model in Sect. 5. Phase transformation in Inconel 718 is not considered in the current work.

## 2 Dynamic strain aging in Inconel 718

The systematic experimental study on Inconel 718 was carried out in [7] under quasi-static compression loading with  $\dot{\epsilon} = 0.001/s$  as well as dynamic compression loading with  $\dot{\epsilon} = 1100/s$  to address the strain rate sensitivity and temperature dependence of the flow stress in Inconel 718. In addition, the various temperatures ranging from 300 to 1200 K were tested along with the above-mentioned strain rates in their work. One of their major observations was that the abnormal bump is generated in the flow stress versus temperature graphs due to DSA as shown in Figs. 1 and 2. Meanwhile, DSA was widely observed in the range of  $600 \text{ K} \lesssim T \lesssim 1000 \text{ K}$  with the quasi-static loading and  $800 \text{ K} \lesssim T \lesssim 1200 \text{ K}$  with the dynamic loading.

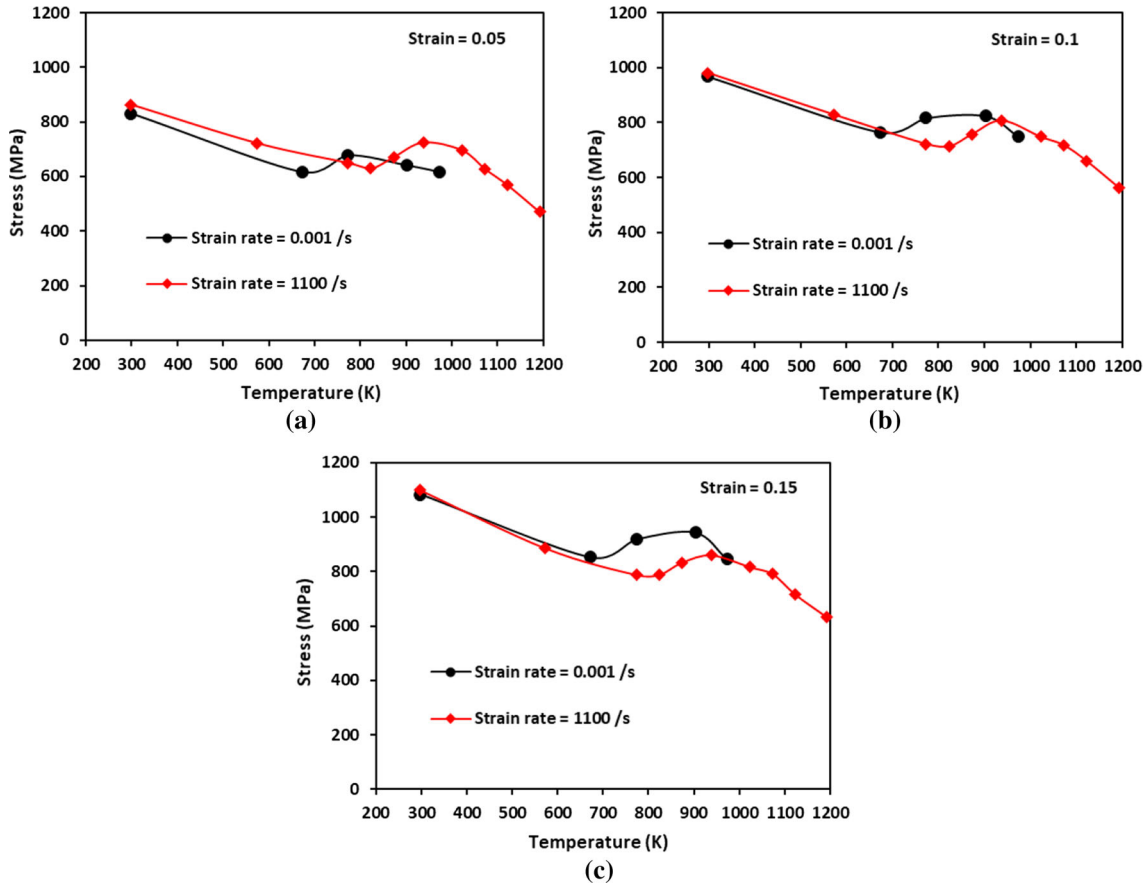


**Fig. 2** Flow stress versus temperature curves from experiments [7] according to the different strain rates with varying strain levels ( $\varepsilon$ ): **a**  $\varepsilon = 0.05$ , **b**  $\varepsilon = 0.1$  and **c**  $\varepsilon = 0.15$

**Table 1** Chemical composition of INCONEL<sup>®</sup> alloy 718 powder (in weight percent, wt%)

Nickel	Chromium	Niobium	Molybdenum	Titanium	Aluminum	Iron
51.75	19.68	4.91	3.18	0.97	0.63	Balance
fcc	bcc	bcc	bcc	hcp	fcc	bcc

It is widely accepted that diffusing solute atoms interact with mobile dislocations, and this interaction becomes the key source of DSA [11]. Physically, DSA is interpreted as the diffusion of solute atoms to the mobile dislocations which are trapped temporarily for a certain amount of time at the obstruction before they move to the next obstruction. When the waiting time of the mobile dislocations becomes identical to the aging time, DSA starts to activate. The aging time  $t_a$  denotes the effective time period for which the dislocations are aged. It was shown that the effective aging time of the dislocations by the solute atoms pinning them is less than the waiting time,  $t_w$ , and therefore it is used to establish the time dependency of the solute atom concentration [12]. The aging time is related to the waiting time as  $dt_a/dt = 1 - t_a/t_w$  [12]. Considering the definition of the waiting time given by the Orowan equation, the aging time  $t_a$  is a function of strain and strain rate history.

In the following section, the constitutive model explaining DSA in Inconel 718 is developed using the concepts of the decomposition of flow stress into athermal and thermal elements, experimental observations, dislocation interaction mechanisms, thermal activation analysis and probability function. The derivations of athermal ( $\sigma_{ath}$ ), thermal ( $\sigma_{th}$ ) and DSA ( $\sigma_w$ ) elements in the flow stress ( $\sigma$ ) in the proposed model are all physically based. For the purpose of modeling DSA, the probability function  $\sigma_w$  is considered as a function of not only the equivalent plastic strain  $\varepsilon_p$  and its rate  $\dot{\varepsilon}_p$  but also the temperature  $T$ . (Details will be given in Sect. 3.2.) This is because the dislocation density depends on the level of the plastic deformation and

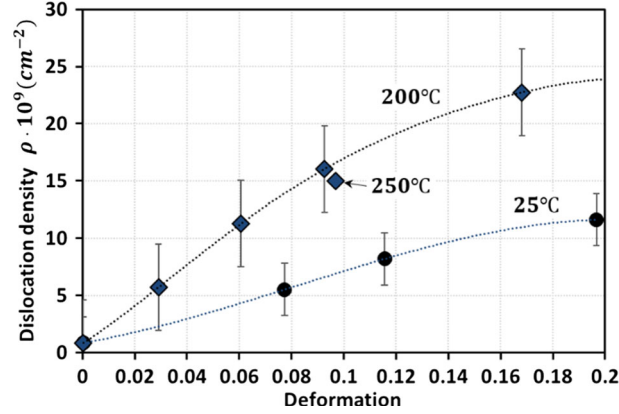


Fig. 3 Dislocation density depending on temperature and strain level [13, 14]

temperature as shown in Fig. 3. As the mathematical expression of the probability function, the Weibull distribution will be employed.

In general, dislocation density tends to decrease with increase in temperature. However, the opposite of this was observed in the experiments by [13] as well as the model predictions by [14] as shown in Fig. 3. The change in the dislocation density with respect to the equivalent plastic strain is given by Eq. (18); correspondingly, the dislocation density is given by Eq. (19) following [14]. As shown in Fig. 4, both the analytical and experimental results show that the values of the parameters  $U - A$  and  $\Omega$  dramatically vary according to the temperature variation during dynamic strain aging. This causes unexpected trend in the values of dislocation density with the temperature variation.

### 3 Constitutive models

In Wang et al. [15], uniaxial compression experiments of a Q235B steel are performed over a wide range of temperature (93–1173 K) and strain rate (0.001–7000/s) and a constitutive model is developed to describe the plastic behavior of the Q235B steel accounting for the DSA effect.

To capture the physical features of DSA, it is important to employ physically based constitutive models which consider the microstructural characteristics of materials as well as the dislocation dynamics, e.g., the models presented by [10, 16–19].

In this section, the physical-/microstructural-based expressions of athermal, thermal and DSA elements of the flow stress are obtained to study the characteristics of Inconel 718 based on the previous works of Voyiadjis and co-workers [9, 10, 17, 20]. In particular, the constitutive model for AL-6XN stainless alloy was proposed in [17] by combining the thermal stress components for bcc and fcc metals since AL-6XN stainless alloy contains a certain amount of fcc and bcc metals, respectively. This idea is employed in the present work since Inconel 718 has similar characteristics as shown in Table 1.

#### 3.1 Athermal and thermal components of flow stress

By studying the dislocation dynamics in metals such as motion, interaction and multiplication of the dislocations, the plastic characteristics of metals can be precisely modeled. The plastic shear strain rate  $\dot{\gamma}^P$  can be calculated by Orowan's relation as follows:

$$\dot{\gamma}^P = b \rho_m v, \quad (1)$$

where  $b$ ,  $\rho_m$  and  $v$  denote the Burgers vector, the density of mobile dislocations and the average velocity of mobile dislocations, respectively.

Following [21], the following relation is assumed:

$$\dot{\epsilon}_{ij}^P = \dot{\gamma}^P M_{ij}, \quad (2)$$

where  $M_{ij}$  denotes the Schmidt orientation tensor and  $\dot{\varepsilon}_{ij}^p$  denotes the plastic strain rate tensor at macroscale.

The Schmidt orientation tensor  $M_{ij}$  is symmetric and defined by

$$M_{ij} = \frac{1}{2}(n_i \otimes s_j + s_i \otimes n_j), \quad (3)$$

where the vectors  $s_i$  and  $n_i$  indicate, respectively, the unit vector in the slip direction and unit normal on the slip plane.

The equivalent plastic strain rate  $\dot{\varepsilon}_p$  can be obtained by substituting of Eq. (1) into Eq. (2) as follows:

$$\dot{\varepsilon}_p = \sqrt{\frac{2}{3} \dot{\varepsilon}_{ij}^p \dot{\varepsilon}_{ij}^p} = \bar{m} b \rho_m v, \quad (4)$$

where the term  $\bar{m}$  denotes the Schmidt orientation factor which is defined by  $\bar{m} = \sqrt{2M_{ij}M_{ij}/3}$ .

Following [22], the evolution of total dislocation density with respect to the equivalent plastic strain can be expressed by

$$\frac{\partial \rho}{\partial \varepsilon_p} = M - k_a(\rho - \rho_i), \quad (5)$$

where  $\varepsilon_p$  denotes the equivalent plastic strain,  $\rho$  and  $\rho_i$  denote the total and initial dislocation densities, respectively,  $M$  denotes the multiplication factor defined by  $M = 1/bl$  with the dislocation mean free path  $l$ , and  $k_a$  denotes the strain rate and temperature-dependent dislocation annihilation factor.

The average dislocation velocity  $v$  is obtained based on the thermally activated process (overcoming local obstructions to dislocation motion). In this work, it is expressed as follows [21]:

$$v = v_0 \exp\left(-\frac{G}{kT}\right), \quad (6)$$

where  $T$  is the absolute temperature,  $k$  denotes the Boltzmann's constant,  $v_0$  is the reference dislocation velocity which is given by  $v_0 = d/t_w$  where  $t_w$  is the waiting time at the obstructions, and  $d$  is the average traveling distance of the dislocation between the obstructions. The term  $G$  denotes the activation energy which may be dependent on the internal structure as well as the shear stress. By following the suggestion of [23], free energy of activation  $G$  is related to the thermal flow stress as follows:

$$G = G_0 \left(1 - \left(\frac{\sigma_{th}}{\hat{\sigma}}\right)^p\right)^q, \quad (7)$$

where the parameters  $p$  and  $q$  define the short-range barriers' shape and  $G_0$  denotes the reference Gibbs energy. The term  $\hat{\sigma}$  stands for the threshold stress ( $\hat{\sigma} = \sigma_{th}$  when  $G = 0$ ).

By the substitution of Eqs. (5) and (6) into Eq. (4) along with Eq. (7), the thermal flow stress  $\sigma_{th}$  can be obtained as follows [9, 10, 17]:

$$\sigma_{th} = \hat{\sigma} \left(1 - \left(\beta_1 T - \beta_2 T \ln \frac{\dot{\varepsilon}_p}{\dot{\varepsilon}_0}\right)^{\frac{1}{q}}\right)^{\frac{1}{p}}, \quad (8)$$

where the term  $\dot{\varepsilon}_0$  denotes the reference strain rate in its initial stage while related to the initial mobile dislocation. In addition, it is needed to maintain the natural logarithmic term unitless. In this work, it is set as 1.0/s.

Meanwhile, the microstructural physics-related terms  $\beta_1$  and  $\beta_2$  are defined, respectively, as follows [9, 10, 17]:

$$\beta_1 = \frac{k}{G_0} \ln \left( \frac{\bar{m} b^2 \rho_m v_0}{b - \bar{m} d (\lambda_1 - b^2 \lambda_2 \rho_m - b \lambda_3 \rho_f^{0.5})} \right), \quad (9)$$

$$\beta_2 = \frac{k}{G_0}, \quad (10)$$

where  $\rho_f$  indicates the forest dislocation density and the coefficients  $\lambda_i$  ( $i = 1 - 3$ ) are related to the immobilization through the interaction between the mobile dislocations and the forest dislocations, the mutual annihilation and trapping of the mobile dislocations, and the multiplication of the mobile dislocations, respectively.

In general, there are two types of barriers which try to block the movements of dislocations in the crystal lattice. The first one is the short-range obstacle due to the forest dislocations, and it can be overcome through the thermal activation energy. Another one is the long-range obstacle due to the material structure, and it cannot be overcome through the thermal activation energy. Thus, the total flow stress ( $\sigma$ ) should be decomposed additively into the thermal ( $\sigma_{th}$ ) and athermal ( $\sigma_{ath}$ ) components as [9, 10, 17]:

$$\sigma = \sigma_{ath} + \sigma_{th}. \quad (11)$$

This assumption of additive decomposition was used and experimentally proven by several works, e.g., [2, 3, 24]. In the present work, based on [9, 10, 17], the following form of athermal flow stress, which is given as a function of  $\varepsilon_p$ , is used:

$$\sigma_{ath}(\varepsilon_p) = Y_a + B_1 \varepsilon_p^{n_1}, \quad (12)$$

where  $Y_a$  indicates the athermal yield stress and the terms  $B_1$  and  $n_1$  indicate the hardening parameters.

Meanwhile, the microstructural components of Inconel 718 contain two types of crystal structures, fcc and bcc, as mentioned earlier. Voyiadjis and Abed proposed a physically based thermal component of flow stress in terms of bcc [10, 25] and fcc [10, 26] as follows:

bcc

$$\sigma_{th}(\dot{\varepsilon}_p, T) = Y_d \left( 1 - \left( \beta_1 T - \beta_2 T \ln \frac{\dot{\varepsilon}_p}{\dot{\varepsilon}_0} \right)^{\frac{1}{q}} \right)^{\frac{1}{p}}, \quad (13)$$

fcc

$$\sigma_{th}(\varepsilon_p, \dot{\varepsilon}_p, T) = B_2 \varepsilon_p^{n_2} \left( 1 - \left( \beta_1 T - \beta_2 T \ln \frac{\dot{\varepsilon}_p}{\dot{\varepsilon}_0} \right)^{\frac{1}{q}} \right)^{\frac{1}{p}}, \quad (14)$$

where the terms  $B_2$  and  $n_2$  indicate the hardening parameters and the parameter  $Y_d$  is the thermal yield stress which is related to the resultant drag stress at the reference velocity.

A combination of Eqs. (13) and (14) is considered in this study to characterize the thermal flow stress of Inconel 718 by following the case of AL-6XN stainless alloy [17]. The formulation of the thermal flow stress component is then given by

$$\sigma_{th}(\varepsilon_p, \dot{\varepsilon}_p, T) = Y_d \left( 1 - \left( \beta_1^Y T - \beta_2^Y T \ln \frac{\dot{\varepsilon}_p}{\dot{\varepsilon}_0} \right)^{\frac{1}{q}} \right)^{\frac{1}{p}} + B_2 \varepsilon_p^{n_2} \left( 1 - \left( \beta_1^H T - \beta_2^H T \ln \frac{\dot{\varepsilon}_p}{\dot{\varepsilon}_0} \right)^{\frac{1}{q}} \right)^{\frac{1}{p}}, \quad (15)$$

where  $\beta_1^Y$ ,  $\beta_1^H$ ,  $\beta_2^Y$  and  $\beta_2^H$  are the microstructural physics-related parameters given in Eqs. (9) and (10). The profound discussion about these parameters is provided in [17]. Meanwhile, the logarithmic plastic strain rate is replaced with the normal plastic strain rate,  $\ln \frac{\dot{\varepsilon}_p}{\dot{\varepsilon}_0} \rightarrow \frac{\dot{\varepsilon}_p}{\dot{\varepsilon}_0}$ , based on [27] in order to acquire a better agreement with the experimental data. Equation (15) becomes

$$\sigma_{th}(\varepsilon_p, \dot{\varepsilon}_p, T) = Y_d \left( 1 - \left( \beta_1^Y T - \beta_2^Y T \frac{\dot{\varepsilon}_p}{\dot{\varepsilon}_0} \right)^{\frac{1}{q}} \right)^{\frac{1}{p}} + B_2 \varepsilon_p^{n_2} \left( 1 - \left( \beta_1^H T - \beta_2^H T \frac{\dot{\varepsilon}_p}{\dot{\varepsilon}_0} \right)^{\frac{1}{q}} \right)^{\frac{1}{p}}. \quad (16)$$

The effect of thermal softening is additionally taken into account in the thermal element of the flow stress for the case of the adiabatic plastic deformations (dynamic loading case). The temperature does not change during the plastic deformation under the isothermal condition (quasi-static loading case), whereas under the



adiabatic plastic deformations, plastic work is converted to heat which leads to the temperature increase inside the material. The temperature increment is calculated as follows [9,10,17]:

$$\Delta T = \frac{\zeta}{c_p \bar{\rho}} \int_0^{\varepsilon_p} \sigma d\varepsilon_p, \quad (17)$$

where  $c_p$  denotes the specific heat capacity at constant pressure and  $\bar{\rho}$  denotes the material density. The term  $\zeta$  denotes the Taylor–Quinney empirical coefficient, and it is assumed as 0.9 in this work as is for most metals [28]. The specific heat capacity  $c_p$  and mass density  $\bar{\rho}$  for Inconel 718 are given by  $c_p = 1.587 \times 10^{-3}$  J/g K and  $\bar{\rho} = 8.19$  g/cm<sup>3</sup> (<http://www.matweb.com>). The temperature is updated during the plastic deformation using Eq. (17). The decrease in flow stress due to the thermal softening is only considered for the dynamic loading ( $\dot{\varepsilon} = 1100$ /s in this work).

Hereafter, the constitutive model containing only the athermal and thermal elements without the DSA component will be referred to as the Voyiadjis–Abed (VA) model [9,10,20], i.e.,  $\sigma_{VA} = \sigma_{ath} + \sigma_{th}$ . On the other hand, the constitutive model containing all the three components to be derived in the following subsection will be referred to as the Voyiadjis–Abed–Song (VAS) model in this work, i.e.,  $\sigma_{VAS} = \sigma_{ath} + \sigma_{th} + \chi\sigma_w$ .

### 3.2 DSA component of flow stress

The change in the dislocation density with respect to the equivalent plastic strain is expressed by [14]

$$\frac{d\rho}{d\varepsilon_p} = U - A - \Omega\rho, \quad (18)$$

where  $U$  denotes the annihilation or immobilization rate of dislocation,  $\Omega$  is related to the probability for annihilation or re-mobilization of immobile dislocations and  $A$  denotes the rate of annihilation of the mobile dislocations. The integration of Eq. (18) gives the expression of dislocation density  $\rho$  as follows:

$$\rho = \frac{U - A}{\Omega} [1 - \exp(-\Omega\varepsilon_p)] + \rho_0 \exp(-\Omega\varepsilon_p), \quad (19)$$

where  $\rho_0$  is the initial dislocation density.

The DSA phenomenon was reported by [14] as shown in Fig. 4. In their work, an increase in stress level ( $\sigma = \alpha\mu b\sqrt{\rho}$ ) or hardening corresponding with the low value of  $\Omega$  and large value of  $U - A$  is observed. From Eq. (19) along with equation  $\sigma = \alpha\mu b\sqrt{\rho}$ , the flow stress can be expressed as

$$\sigma = \sigma_0 + \alpha\mu b \left\{ \frac{U - A}{\Omega} [1 - \exp(-\Omega\varepsilon_p)] + \rho_0 \exp(-\Omega\varepsilon_p) \right\}^{1/2}, \quad (20)$$

where  $\sigma_0$  is the strain-independent friction stress,  $\mu$  is the shear modulus and  $\alpha$  is the material constant. In this context, it is obvious that DSA has the probabilistic nature of physical phenomenon and can be characterized through a probability function.

To model DSA, an additional probability function  $\sigma_w$  is introduced based on the above discussion. It is assumed that the function  $\sigma_w$  depends on the equivalent plastic strain ( $\varepsilon_p$ ), its corresponding rate ( $\dot{\varepsilon}$ ) and temperature ( $T$ ). Therefore, the constitutive relation in the VAS model can be expressed as

$$\sigma_{VAS}(\varepsilon_p, \dot{\varepsilon}_p, T) = \sigma_{ath}(\varepsilon_p) + \sigma_{th}(\varepsilon_p, \dot{\varepsilon}_p, T) + \chi\sigma_w(\varepsilon_p, \dot{\varepsilon}_p, T), \quad (21)$$

where the first two terms on the right-hand side are the athermal and thermal elements of the flow stress, respectively, given by Eqs. (12) and (16) and the coefficient  $\chi$  is related to the DSA. Since DSA is activated only at the specific combinations of temperature and strain rate conditions, the use of the coefficient  $\chi$  is inevitable so as to define the activation range of DSA. The inactivated DSA condition which corresponds to the VA model can be recovered when  $\chi = 0$ , whereas the full consideration of DSA can be achieved with the condition  $\chi = 1$ . The coefficient  $\chi$  is defined as a function of temperature as follows:

$$\chi(T) = \frac{1}{4} \left( 1 + \tanh \frac{T - T_l}{\xi} \right) \left( 1 - \tanh \frac{T - T_u}{\xi} \right), \quad (22)$$

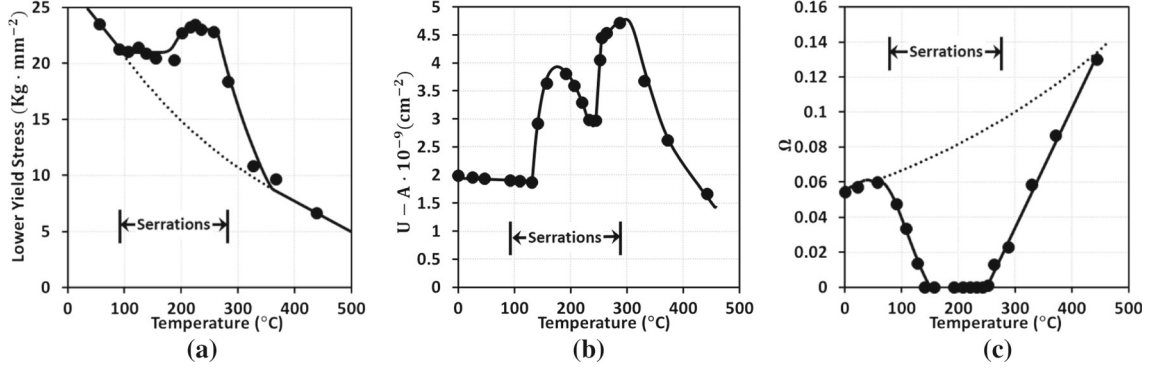


**Fig. 4** Comparison between experimental data and model predictions in terms of: **a** lower yield stress, **b**  $U - A$  and **c**  $\Omega$ . Dots and lines represent experimental data and model predictions, respectively [14]

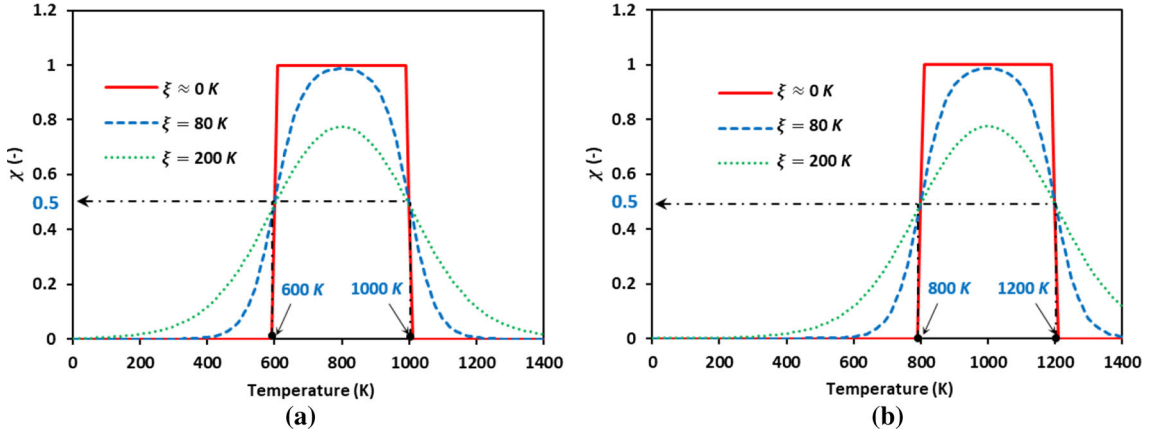


**Fig. 5** Coefficient  $\chi$  as a function of temperature and the parameter  $\xi$  with **a** quasi-static loading (0.001/s) and **b** dynamic loading (1100/s)

where the parameters  $T_u$  and  $T_l$  are the upper and lower limits of temperature range where DSA is active, and the parameter  $\xi$  controls smoothness of  $\chi$  and is temperature-dimensioned. As mentioned previously in Sect. 2, in the experiments of [7]. In [8], quasi-static loadings ( $\dot{\epsilon} = 0.0015/s$  and  $0.15/s$ ) were investigated; in turn, DSA was observed in the same, single range of temperature. However, in the current work, dynamic loading is also considered. DSA in Inconel 718 is observed in the range of  $600 \text{ K} \lesssim T \lesssim 1000 \text{ K}$  in the quasi-static loading, whereas  $800 \text{ K} \lesssim T \lesssim 1200 \text{ K}$  in the dynamic loading. Therefore, two sets of the parameters ( $T_l$ ,  $T_u$ ) are used in this work depending on the applied strain rate. Figure 5 shows the graphs of the coefficient  $\chi$  as a function of temperature with the three different values of  $\xi$  for the quasi-static loading and the dynamic loading. In Fig. 5a, the three curves intersect at (600 K, 0.5) and (1000 K, 0.5). In Fig. 5b, the three curves intersect at (800 K, 0.5) and (1200 K, 0.5). For the physically reasonable changeover of DSA,  $\xi = 80 \text{ K}$  is selected for both the quasi-static and dynamic loading conditions in this work.

The standard parametrization form of the Weibull distribution probability density function is employed to define the DSA-induced component of flow stress  $\sigma_w$  as follows:

$$\sigma_w(\varepsilon_p, \dot{\varepsilon}_p, T) = a_w \exp \left[ - \frac{\{T - \mathcal{W}(\dot{\varepsilon}_p)\}^2}{b_w} \right], \quad (23)$$

where the shapes and scales of the Weibull distribution probability density function are determined by the terms  $a_w(\varepsilon_p) > 0$  and  $b_w(\varepsilon_p) > 0$ . The expressions for  $a_w$ ,  $b_w$  and  $\mathcal{W}(\varepsilon_p)$  will be obtained in the following section based on the experiments of [7]. Moreover, the material parameters for defining the athermal and thermal components of flow stress will be obtained in Sect. 4.



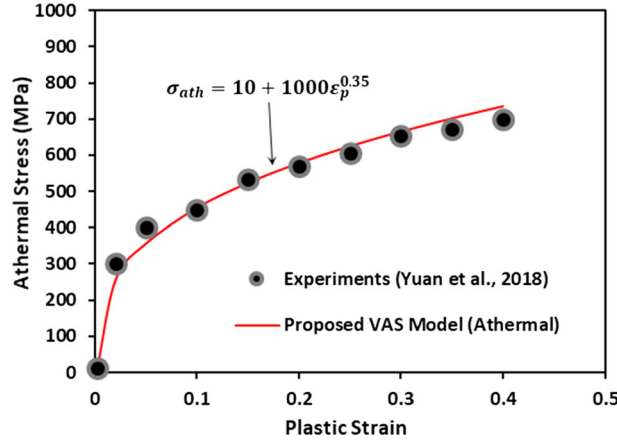


**Fig. 6** Athermal flow stress versus plastic strain responses from the experiments [7] and the VAS model (Eq. 12)

**Table 2** Material parameters used to define the athermal and thermal flow stresses for Inconel 718

$Y_a$ (MPa)	$B_1$ (MPa)	$n_1$ (—)	$Y_d$ (MPa)	$B_2$ (MPa)	$n_2$ (—)
10	1000	0.35	900	600	0.43
$\beta_1^Y$ (1/K)	$\beta_2^Y$ (1/K)	$\beta_1^H$ (1/K)	$\beta_2^H$ (1/K)	$p$ (—)	$q$ (—)
$9.0 \times 10^{-4}$	$6.0 \times 10^{-8}$	$1.8 \times 10^{-4}$	$3.1 \times 10^{-8}$	0.5	1.5

#### 4 Model calibrations and comparisons for DSA

The model calibration procedure starts by using the stress–temperature curves such as Figs. 1 and 2 with different values of strain rate and plastic strain. Generally, the flow stress tends to decrease with the temperature increase until a certain level of temperature, and then it keeps constant. That unchanging level of stress stands for the athermal component of flow stress,  $\sigma_{ath}$ . Using the athermal flow stress in the stress–temperature curves with different values of plastic strain, the three parameters ( $Y_a$ ,  $B_1$  and  $n_1$ ) in Eq. (12) are obtained as shown in Fig. 6.

The thermal flow stress  $\sigma_{th}$  can be determined by the equation  $\sigma_{th} = \sigma - \sigma_{ath}$  without considering DSA. The suitable values of the parameters,  $p$  and  $q$ , lead to appropriately capture the thermal degradation mechanism. Typically, these parameters are in the following ranges:  $p \in [0 : 1]$  and  $q \in [1 : 2]$ . The parameters  $p = 0.5$  and  $q = 1.5$  are selected in this work by following [10, 17]. To obtain the thermal yield stress  $Y_d$ , the flow stress at initial yield point  $\sigma_{\varepsilon_p=0}$  is employed. From Eqs. (12) and (16), one can obtain  $Y_d$  by plotting  $(\sigma_{\varepsilon_p=0} - Y_a)^p$  versus  $T^{\frac{1}{q}}$  graph for each strain rate. The graph of  $(1 - ((\sigma_{\varepsilon_p=0} - Y_a)/Y_d)^p)^q$  versus  $\dot{\varepsilon}_p$  at certain temperature is used to obtain the parameters  $\beta_1^Y$  and  $\beta_2^Y$ . Similarly, the graphs of  $(\sigma - Y_d(1 - (\beta_1^Y T - \beta_2^Y T \frac{\dot{\varepsilon}_p}{\dot{\varepsilon}_0})^{1/q})^{1/p} - Y_a - B_1 \varepsilon_p^{n_1})^p$  versus  $T^{\frac{1}{q}}$  at several levels of plastic strain along with a certain strain rate are used to obtain the parameters  $B_2$  and  $n_2$ . Lastly, the graphs of  $(1 - ((\sigma - Y_d(1 - (\beta_1^Y T - \beta_2^Y T \frac{\dot{\varepsilon}_p}{\dot{\varepsilon}_0})^{1/q})^{1/p} - Y_a - B_1 \varepsilon_p^{n_1})/B_2 \varepsilon_p^{n_2})^p)^q$  versus  $\dot{\varepsilon}_p$  at certain temperature and plastic strain are used to obtain the parameters  $\beta_1^H$  and  $\beta_2^H$ . More detailed procedure to obtain material parameters is given in [17]. From the procedure above, the material parameters for Inconel 718 used in the VA model (without the DSA-induced stress) are obtained and listed in Table 2.

Next, the expressions of  $a_w$ ,  $b_w$  and  $\mathcal{W}$  in Eq. (23) need to be obtained to define the DSA component of flow stress. As shown in Figs. 1 and 2, the bulges due to DSA are observed in all of the stress–temperature experimental curves with the two different strain rates ( $\dot{\varepsilon} = 0.001/s$  and  $1100/s$ ). These experimental series are utilized to find the expressions of  $a_w$ ,  $b_w$  and  $\mathcal{W}$ . In this work, an elastic regime is assumed to be negligibly small, i.e.,  $\varepsilon = \varepsilon_p$ . In addition, it is assumed  $\dot{\varepsilon} = \dot{\varepsilon}_p$ . By comparing the DSA-induced flow stress obtained by Eq. (23) with the experimental data, the parameters  $a_w$  and  $b_w$  can be obtained as shown in Fig. 7. From the calibration process, it is discovered that these two parameters are independent of the strain rate, but are

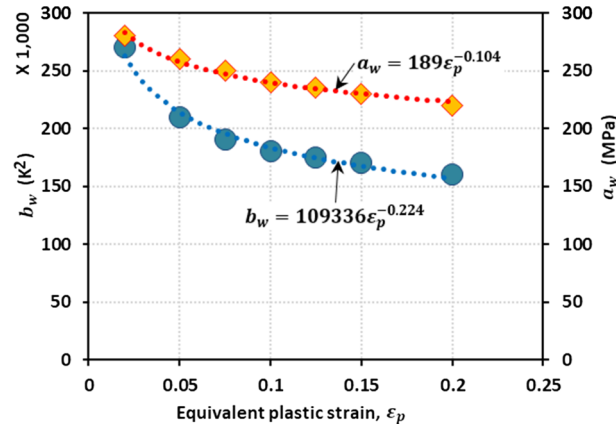


Fig. 7 Plots of  $a_w$  and  $b_w$  with respect to  $\varepsilon_p$ . The trend lines using a power law are displayed as the dotted lines for both parameters

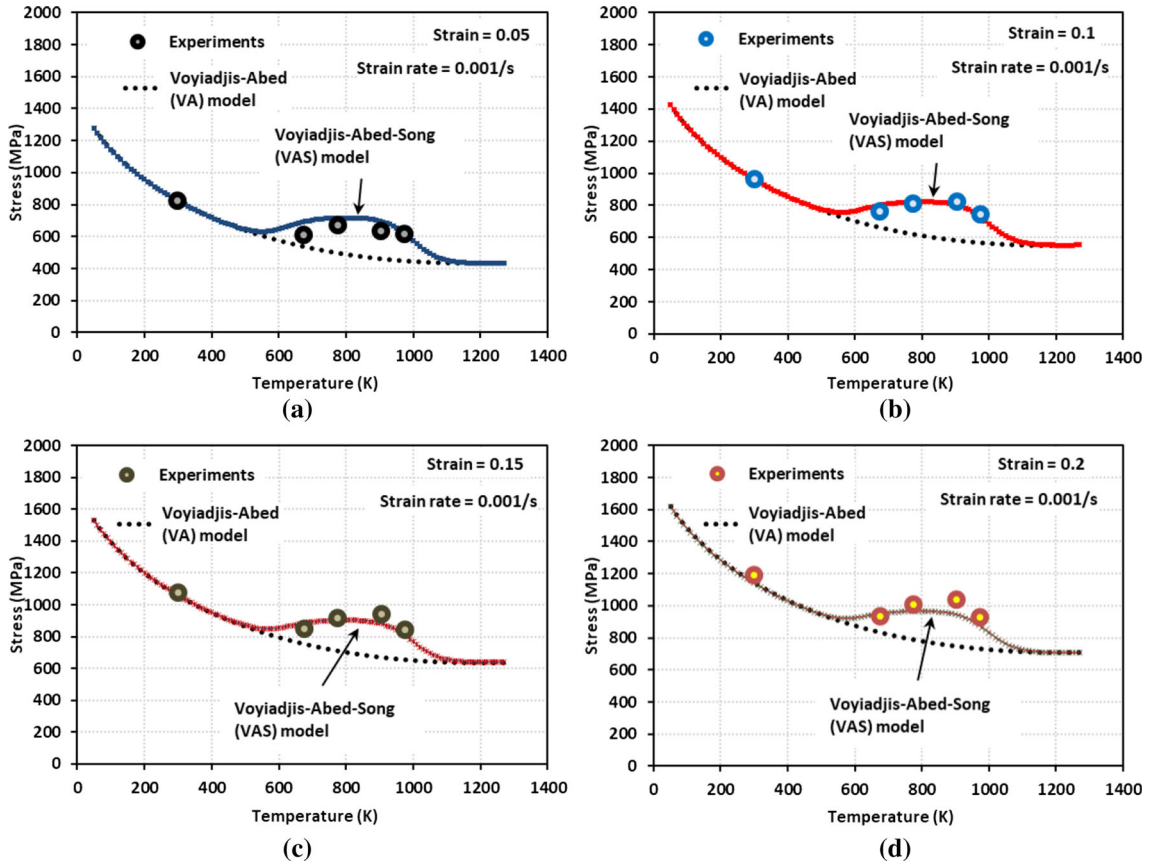
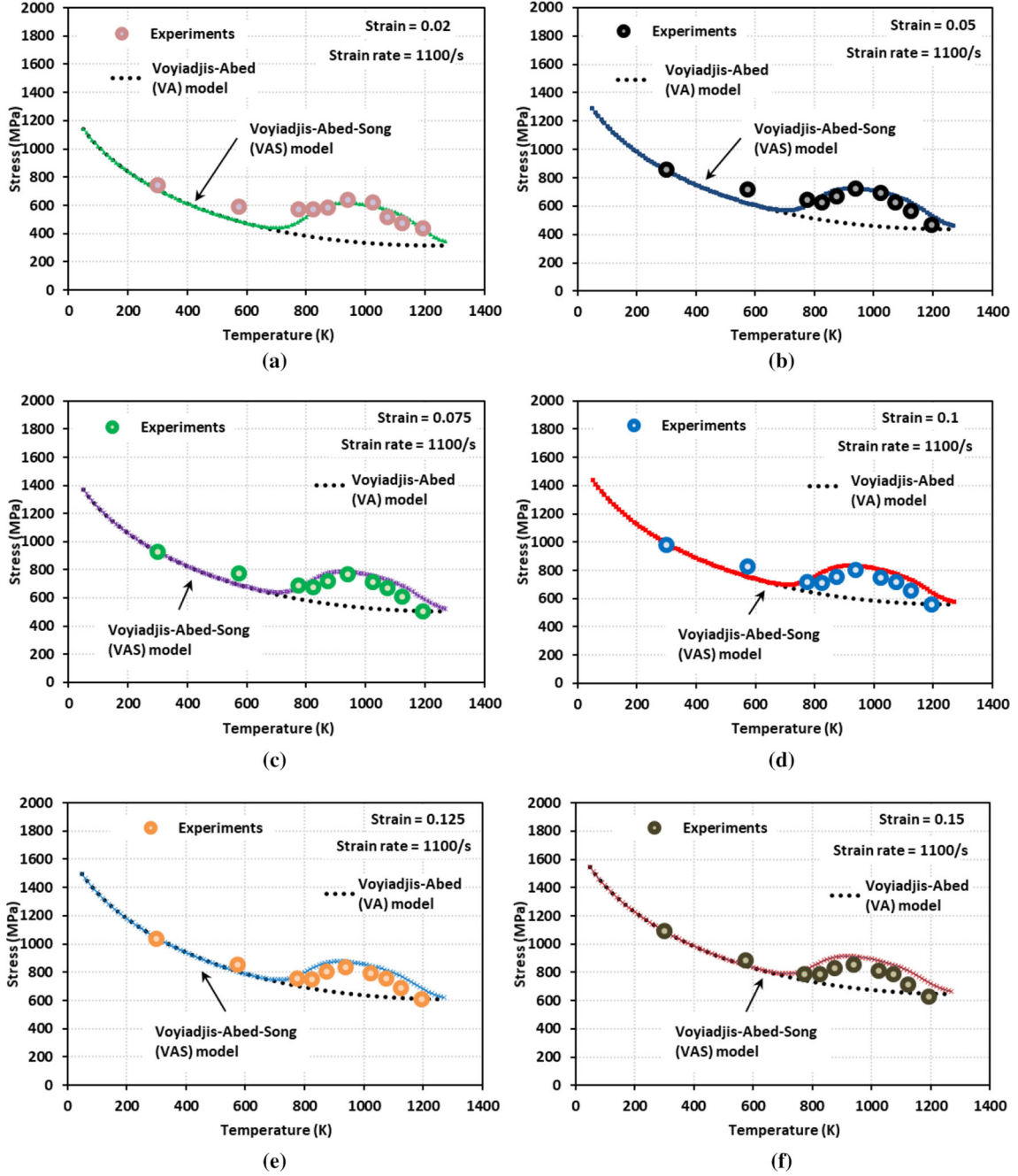


Fig. 8 Flow stress versus temperature curves of the VA and VAS models along with the experimental data [7] at the following levels of strain: **a**  $\varepsilon = 0.05$ , **b**  $\varepsilon = 0.10$ , **c**  $\varepsilon = 0.15$  and **d**  $\varepsilon = 0.20$ . Quasi-static loading with  $\dot{\varepsilon} = 0.001/s$  is applied

dependent on the equivalent plastic strain. The obtained expressions for  $a_w$  and  $b_w$  are as follows:

$$a_w = 189\varepsilon_p^{-0.104} \text{ (MPa)}, \quad (24)$$

$$b_w = 109336\varepsilon_p^{-0.224} \text{ (K}^2\text{)}. \quad (25)$$



**Fig. 9** Flow stress versus temperature curves of the VA and VAS models along with the experimental data [7] at the following levels of strain: **a**  $\epsilon = 0.02$ , **b**  $\epsilon = 0.05$ , **c**  $\epsilon = 0.075$ , **d**  $\epsilon = 0.10$ , **e**  $\epsilon = 0.125$  and **f**  $\epsilon = 0.15$ . Dynamic loading with  $\dot{\epsilon} = 1100/s$  is applied

Meanwhile, many data sets were available to determine  $a_W$  and  $b_W$  as shown in Figs. 1, 2 and 7. However, when it comes to the strain rate-dependent function  $\mathcal{W}$ , only two data sets are available to obtain the function  $\mathcal{W}$  according to the strain rates (0.001/s and 1100/s). Thus, it is unfeasible to obtain the unique expression for this function. From the experimental data, the following plausible forms of the function  $\mathcal{W}$  can be obtained:

$$\mathcal{W}(\dot{\epsilon}) = 933 - 2.49 \ln \frac{\dot{\epsilon}_p}{\dot{\epsilon}_0}, \quad (26)$$

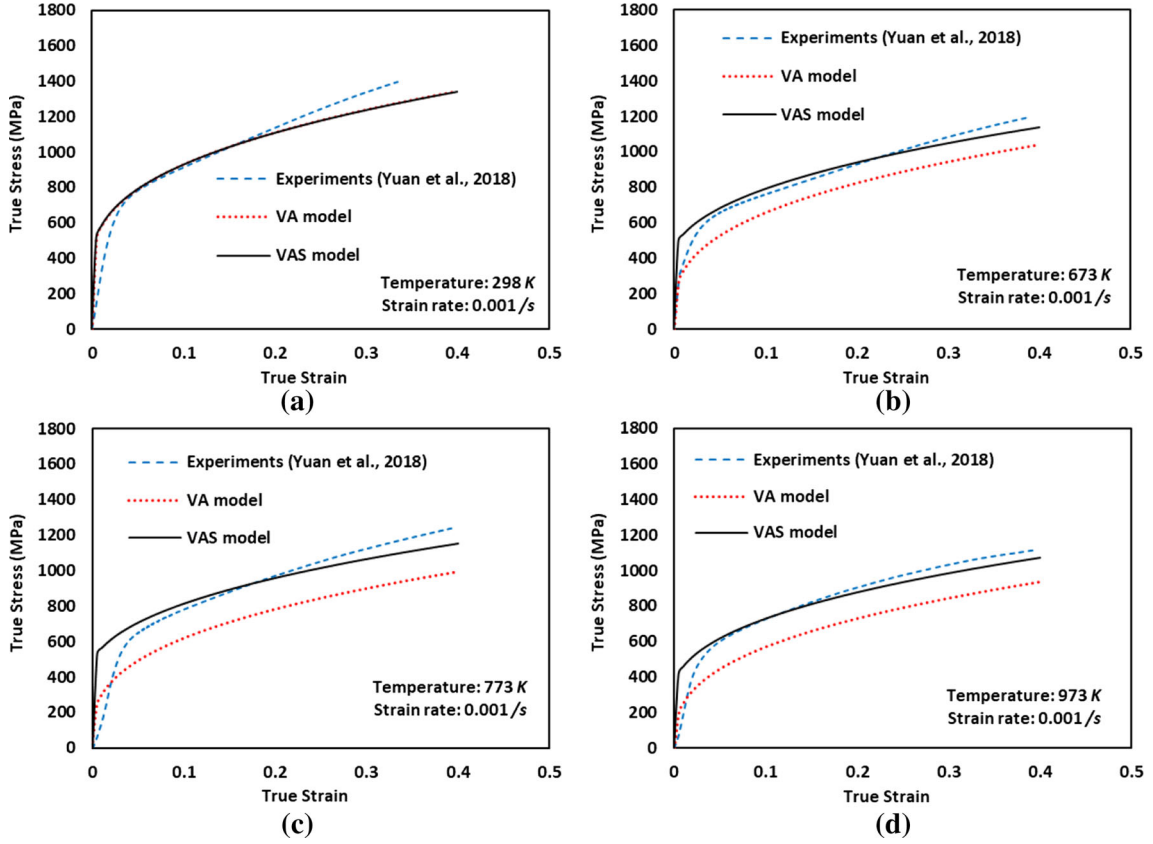


**Fig. 10** Flow stress versus strain curves of the VA and VAS models along with the experimental data [7] at the following temperatures: **a**  $T = 298$  K, **b**  $T = 673$  K, **c**  $T = 773$  K and **d**  $T = 973$  K. Quasi-static loading with  $\dot{\epsilon} = 0.001/s$  is applied

$$\mathcal{W}(\dot{\epsilon}) = 933 \left( \frac{\dot{\epsilon}_p}{\dot{\epsilon}_0} \right)^{-0.003}, \quad (27)$$

$$\mathcal{W}(\dot{\epsilon}) = 950 - 0.0315 \frac{\dot{\epsilon}_p}{\dot{\epsilon}_0}. \quad (28)$$

Among these equations, Eq. (27) is employed in this work since it gives better correlation with the data with fewer terms. Substituting Eqs. (24), (25) and (27) into Eq. (23), the DSA component of flow stress  $\sigma_w$  is expressed as follows:

$$\sigma_w(\epsilon_p, \dot{\epsilon}_p, T) = 189 \epsilon_p^{-0.104} \exp \left[ -\frac{\{T - 933(\dot{\epsilon}_p/\dot{\epsilon}_0)^{-0.003}\}^2}{109336 \epsilon_p^{-0.224}} \right]. \quad (29)$$

Finally, the VAS model for Inconel 718 is given by substituting Eqs. (13), (16), (22) and (29) into Eq. (21) as follows:

$$\begin{aligned} \sigma_{\text{VAS}}(\epsilon_p, \dot{\epsilon}_p, T) = & Y_a + B_1 \epsilon_p^{n_1} + Y_d \left( 1 - \left( \beta_1^Y T - \beta_2^Y T \frac{\dot{\epsilon}_p}{\dot{\epsilon}_0} \right)^{\frac{1}{q}} \right)^{\frac{1}{p}} \\ & + B_2 \epsilon_p^{n_2} \left( 1 - \left( \beta_1^H T - \beta_2^H T \frac{\dot{\epsilon}_p}{\dot{\epsilon}_0} \right)^{\frac{1}{q}} \right)^{\frac{1}{p}} \\ & + \frac{189}{4} \left( 1 + \tanh \frac{T - T_l}{\xi} \right) \left( 1 - \tanh \frac{T - T_u}{\xi} \right) \epsilon_p^{-0.104} \end{aligned}$$

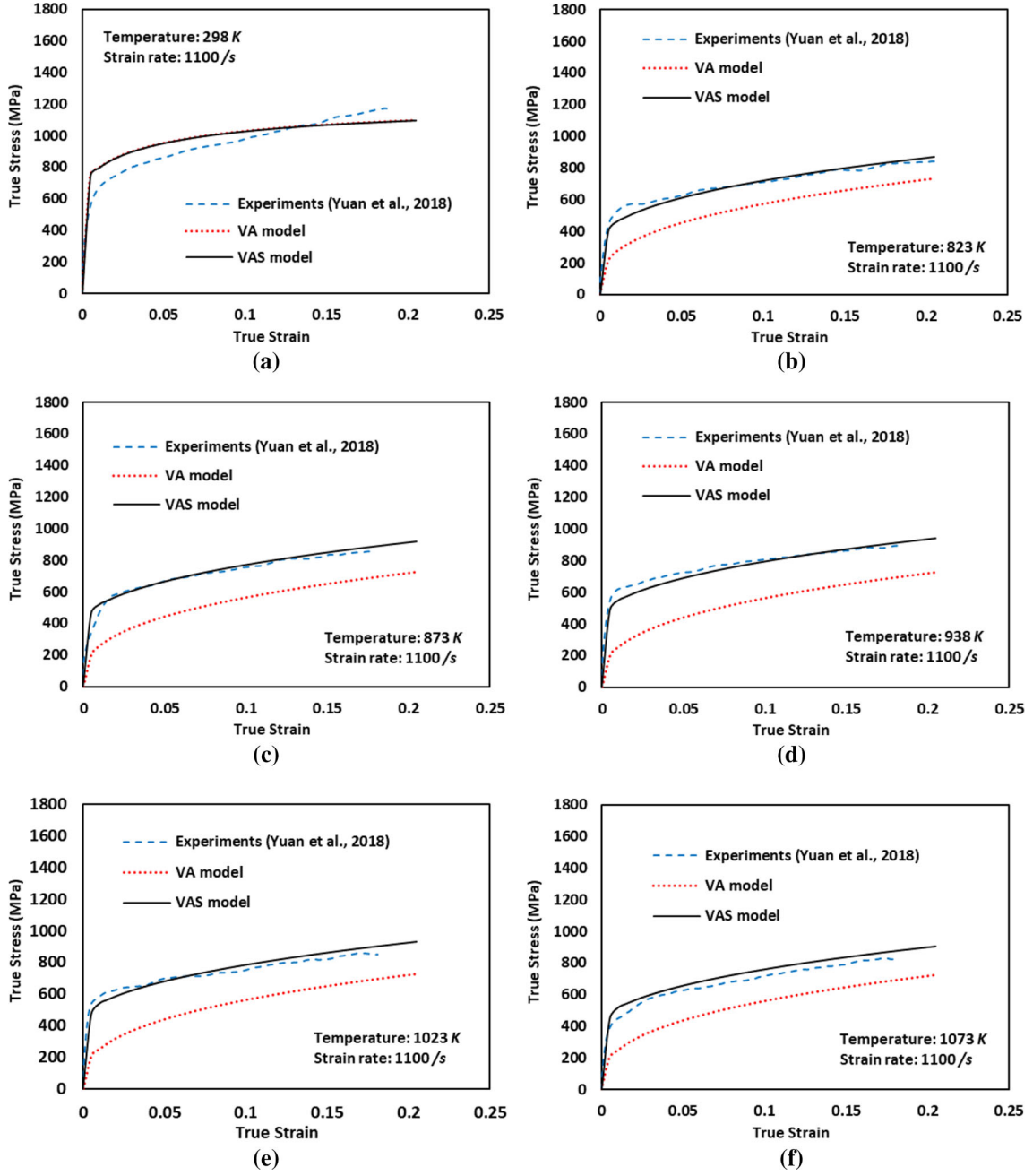


**Fig. 11** Flow stress versus strain curves of the VA and VAS models along with the experimental data [7] at the following temperatures: **a**  $T = 298$  K, **b**  $T = 823$  K, **c**  $T = 873$  K, **d**  $T = 938$  K, **e**  $T = 1023$  K and **(f)**  $T = 1073$  K. Dynamic loading with  $\dot{\epsilon} = 1100/s$  is applied

$$\exp \left[ - \frac{\left\{ T - 933 (\dot{\epsilon}_p / \dot{\epsilon}_0)^{-0.003} \right\}^2}{109336 \epsilon_p^{-0.224}} \right]. \quad (30)$$

The flow stresses predicted by the VA model and VAS model along with the experimental measurements are shown in Fig. 8 (quasi-static loading) and Fig. 9 (dynamic loading) according to the varying applied strain rates. Contrary to the VA model, the VAS model demonstrates its ability to capture the (bulge-shaped) work hardening due to the DSA through these figures.

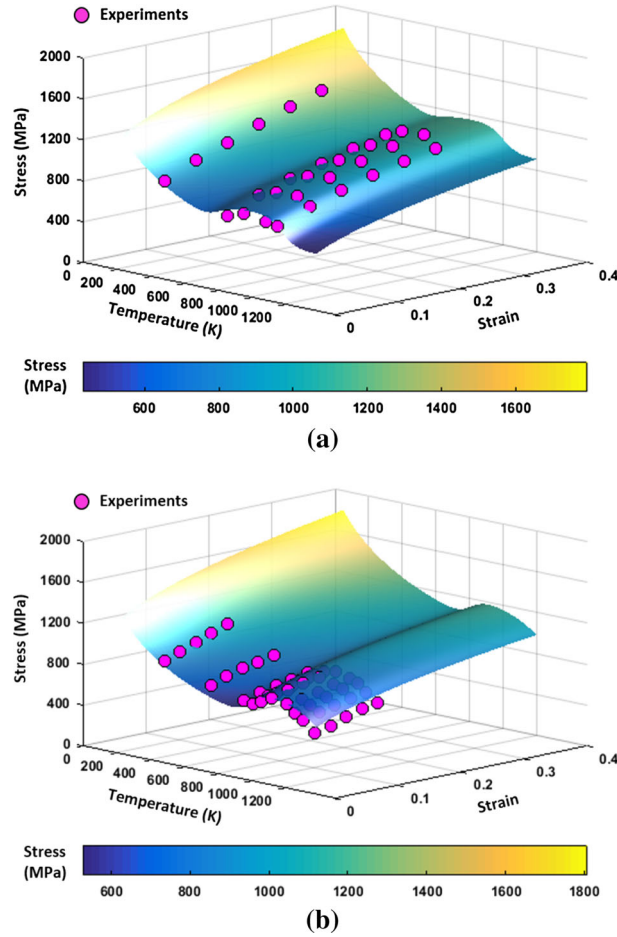


**Fig. 12** Surfaces of the total flow stress as a function of temperature and strain level from the VAS model with two strain rates: **a**  $\dot{\epsilon} = 0.001/s$  and **b**  $\dot{\epsilon} = 1100/s$ . The experimental data are from [7]

## 5 Comparisons between experiments and VAS model

As shown in Figs. 8 and 9, both the VA and VAS models successfully capture the experimental observations in the low range of temperatures (DSA free), whereas, when DSA becomes active, the VA model is not able to capture the experiments.

The experimental stress–strain curves given by [7] are considered in this section. Both models are directly compared with experiments. Figure 10 shows the flow stress–strain responses at the different temperatures with the quasi-static loading ( $\dot{\epsilon} = 0.001/s$ ). As mentioned earlier, the experiments are well captured by both the VA and VAS models when DSA is inactive (Fig. 10a). On the other hand, when DSA activates, the VA model is not able to capture the experiments as shown in Figs. 10b–d, while the VAS model is able to capture the DSA-induced additional hardening. Figure 11 shows the flow stress–strain responses at the different temperatures with the dynamic loading ( $\dot{\epsilon} = 1100/s$ ). Similar trend is observed in this loading case. When DSA is inactive (Fig. 11a), the VA model can accurately predict the experiments; however, it shows significant underestimates when DSA becomes active (Figs. 11b–f).

The surfaces of the total flow stress with the two strain rates are presented in Fig. 12 at a wide range of temperatures ( $T = 0 - 1200$  K) and strain levels ( $\epsilon = 0 - 0.4$ ). The experimental measurements are also plotted mostly near the surfaces.



## 6 Conclusions

The dynamic strain aging phenomenon was observed in the experimental works of [7] for Inconel 718. The existing Johnson–Cook model or the Voyiadjis–Abed model cannot capture the dynamic strain aging phenomenon. In general, dynamics strain aging is recognized as an outcome of the interaction between mobile dislocations and diffusing solute atoms; nevertheless, its physics is still vague. The previous model of the authors [17] is modified in this work using the Weibull distribution probability density function, and this modification is physics-based through an evolution of the dislocation density. From the comparisons with the experiments of [7], it is demonstrated that the proposed VAS model is able to capture the DSA phenomenon observed in a wide range of temperatures with different strain rates in Inconel 718. Lastly, it is worth mentioning that the proposed VAS model is easy and straightforward to implement in the existing finite element algorithms.

**Acknowledgements** The financial support provided by a grant from the National Science Foundation EPSCoR CIMM (Grant Number #OLA-1541079) is gratefully acknowledged. The authors also acknowledge experimental data on Inconel 718 superalloy provided to the authors by Professor Weiguo Guo at Northwestern Polytechnical University, People’s Republic of China.

## References

1. Wang, X.Y., Huang, C.Z., Zou, B., Liu, H.L., Zhu, H.T., Wang, J.: Dynamic behavior and a modified Johnson–Cook constitutive model of Inconel 718 at high strain rate and elevated temperature. *Mater. Sci. Eng. Struct.* **580**, 385–390 (2013). <https://doi.org/10.1016/j.msea.2013.05.062>
2. Nemat-Nasser, S., Isaacs, J.B.: Direct measurement of isothermal flow stress of metals at elevated temperatures and high strain rates with application to Ta and Ta-W alloys. *Acta Mater.* **45**(3), 907–919 (1997). [https://doi.org/10.1016/S1359-6454\(96\)00243-1](https://doi.org/10.1016/S1359-6454(96)00243-1)
3. Nemat-Nasser, S., Guo, W.G., Cheng, J.Y.: Mechanical properties and deformation mechanisms of a commercially pure titanium. *Acta Mater.* **47**(13), 3705–3720 (1999). [https://doi.org/10.1016/S1359-6454\(99\)00203-7](https://doi.org/10.1016/S1359-6454(99)00203-7)
4. Candioto, K.C.G., Caliarì, F.R., Reis, D.A.P., Couto, A.A., Nunes, C.A.: Characterization of the superalloy Inconel 718 after double aging heat treatment. In: Öchsner A., Altenbach H. (eds.) *Mechanical and Materials Engineering of Modern Structure and Component Design*, *Advanced Structured Materials*, vol 70. pp. 293–300. Springer, Cham (2015)
5. Mulford, R.A., Kocks, U.F.: New observations on the mechanisms of dynamic strain aging and of Jerky flow. *Acta Metall. Mater.* **27**(7), 1125–1134 (1979). [https://doi.org/10.1016/0001-6160\(79\)90130-5](https://doi.org/10.1016/0001-6160(79)90130-5)
6. Nalawade, S.A., Sundararaman, M., Kishore, R., Shah, J.G.: The influence of aging on the serrated yielding phenomena in a nickel-base superalloy. *Scr. Mater.* **59**(9), 991–994 (2008). <https://doi.org/10.1016/j.scriptamat.2008.07.004>
7. Yuan, K.B., Guo, W.G., Li, P.H., Wang, J.J., Su, Y., Lin, X., Li, Y.P.: Influence of process parameters and heat treatments on the microstructures and dynamic mechanical behaviors of Inconel 718 superalloy manufactured by laser metal deposition. *Mater. Sci. Eng. Struct.* **721**, 215–225 (2018). <https://doi.org/10.1016/j.msea.2018.02.014>
8. Voyiadjis, G.Z., Song, Y., Rusinek, A.: Constitutive model for metals with dynamic strain aging. *Mech. Mater.* **129**, 352–360 (2019). <https://doi.org/10.1016/j.mechmat.2018.12.012>
9. Abed, F.H., Voyiadjis, G.Z.: A consistent modified Zerilli–Armstrong flow stress model for BCC and FCC metals for elevated temperatures. *Acta Mech.* **175**(1–4), 1–18 (2005). <https://doi.org/10.1007/s00707-004-0203-1>
10. Voyiadjis, G.Z., Abed, F.H.: Microstructural based models for BCC and FCC metals with temperature and strain rate dependency. *Mech. Mater.* **37**(2–3), 355–378 (2005). <https://doi.org/10.1016/j.mechmat.2004.02.003>
11. Cottrell, A.H.: A note on the Portevin–Le Chatelier effect. *Philos. Mag.* **44**(355), 829–832 (1953)
12. McCormick, P.G.: Theory of flow localization due to dynamic strain aging. *Acta Metall. Mater.* **36**(12), 3061–3067 (1988). [https://doi.org/10.1016/0001-6160\(88\)90043-0](https://doi.org/10.1016/0001-6160(88)90043-0)
13. Keh, A., Nakada, Y., Leslie, W.: *Dislocation Dynamics*, pp. 81–87. McGraw Hill, New York (1968)
14. Bergstrom, Y., Roberts, W.: Application of a dislocation model to dynamical strain ageing in alpha-iron containing interstitial atoms. *Acta Metall. Mater.* **19**(8), 815–823 (1971). [https://doi.org/10.1016/0001-6160\(71\)90138-6](https://doi.org/10.1016/0001-6160(71)90138-6)
15. Wang, J.J., Guo, W.G., Gao, X.S., Su, J.: The third-type of strain aging and the constitutive modeling of a Q235B steel over a wide range of temperatures and strain rates. *Int. J. Plast.* **65**, 85–107 (2015). <https://doi.org/10.1016/j.ijplas.2014.08.017>
16. Rusinek, A., Klepaczko, J.R.: Shear testing of a sheet steel at wide range of strain rates and a constitutive relation with strain-rate and temperature dependence of the flow stress. *Int. J. Plast.* **17**(1), 87–115 (2001). [https://doi.org/10.1016/S0749-6419\(00\)00020-6](https://doi.org/10.1016/S0749-6419(00)00020-6)
17. Abed, F.H., Voyiadjis, G.Z.: Plastic deformation modeling of AL-6XN stainless steel at low and high strain rates and temperatures using a combination of BCC and FCC mechanisms of metals. *Int. J. Plast.* **21**(8), 1618–1639 (2005). <https://doi.org/10.1016/j.ijplas.2004.11.003>
18. Rusinek, A., Zaera, R., Klepaczko, J.R.: Constitutive relations in 3-D for a wide range of strain rates and temperatures—application to mild steels. *Int. J. Solids Struct.* **44**(17), 5611–5634 (2007). <https://doi.org/10.1016/j.ijsolstr.2007.01.015>
19. Klepaczko, J.R., Rusinek, A., Rodriguez-Martinez, J.A., Pecherski, R.B., Arias, A.: Modelling of thermo-viscoplastic behaviour of DH-36 and Weldox 460-E structural steels at wide ranges of strain rates and temperatures, comparison of constitutive relations for impact problems. *Mech. Mater.* **41**(5), 599–621 (2009). <https://doi.org/10.1016/j.mechmat.2008.11.004>

20. Voyiadjis, G.Z., Abed, F.H.: Effect of dislocation density evolution on the thermomechanical response of metals with different crystal structures at low and high strain rates and temperatures. *Arch. Mech.* **57**(4), 299–343 (2005)
21. Bammann, D.J., Aifantis, E.C.: On a proposal for a continuum with microstructure. *Acta. Mech.* **45**(1–2), 91–121 (1982). <https://doi.org/10.1007/Bf01295573>
22. Klepaczko, J.R.: Modelling of structural evolution at medium and high strain rates, FCC and BCC metals. In: *Constitutive Relations and Their Physical Basis*, pp. 387–395 (1987)
23. Kocks, U.F., Argon, A.S., Ashby, M.F.: Thermodynamics and kinetics of slip. *Prog. Mater. Sci.* **19**, 1–281 (1975)
24. Zerilli, F.J., Armstrong, R.W.: Dislocation-mechanics-based constitutive relations for material dynamics calculations. *J. Appl. Phys.* **61**(5), 1816–1825 (1987). <https://doi.org/10.1063/1.338024>
25. Voyiadjis, G.Z., Abed, F.H.: A coupled temperature and strain rate dependent yield function for dynamic deformations of BCC metals. *Int. J. Plast.* **22**(8), 1398–1431 (2006). <https://doi.org/10.1016/j.ijplas.2005.10.005>
26. Voyiadjis, G.Z., Abed, F.H.: Implicit algorithm for finite deformation hypoelastic-viscoplasticity in FCC metals. *Int. J. Numer. Meth. Eng.* **67**(7), 933–959 (2006). <https://doi.org/10.1002/nme.1655>
27. Simon, P., Demarty, Y., Rusinek, A., Voyiadjis, G.Z.: Material behavior description for a large range of strain rates from low to high temperatures: application to high strength steel. *Metals* **8**(10), 795 (2018)
28. Rittel, D., Zhang, L.H., Osovski, S.: The dependence of the Taylor–Quinney coefficient on the dynamic loading mode. *J. Mech. Phys. Solids* **107**, 96–114 (2017). <https://doi.org/10.1016/j.jmps.2017.06.016>

**Publisher’s Note** Springer Nature remains neutral with regard to jurisdictional claims in published maps and institutional affiliations.